POLITECNICO DI TORINO
Repository ISTITUZIONALE

Augmented Iconography.
AR applications to the fortified Turin in the Theatrum Sabaudiae

Original
Augmented Iconography.
AR applications to the fortified Turin in the Theatrum Sabaudiae / Palma, V.; Lo Turco, M.; Spallone, R.; Vitali, M.. - ELETTRONICO. - (2018), pp. 155-155. (Intervento presentato al convegno INTERNATIONAL CONFERENCE ON MODERN AGE FORTIFICATIONS OF THE MEDITERRANEAN COAST tenutosi a Torino nel 18th, 19th, 20th October 2018).

Availability:
This version is available at: 11583/2714984 since: 2018-10-11T15:50:36Z

Publisher:
Politecnico di Torino

Published
DOI:

Terms of use:

This article is made available under terms and conditions as specified in the corresponding bibliographic description in the repository

Publisher copyright

(Article begins on next page)

25 April 2024

JOURNAL OF MATERIALS RESEARCH AND TECHNOLOGY 2022;21:4200–4211

Available online at www.sciencedirect.com

jmr&t
Journal of Materials Research and Technology

journal homepage: www.elsevier.com/locate/jmrt

Original Article

Work hardening behavior and substructure evolution of a low-density steel during compressive deformation

Aida Azizi [a], *Hamid Reza Abedi* [a,*], *Abdollah Saboori* [b]

[a] *School of Metallurgy & Materials Engineering, Iran University of Science and Technology (IUST), Tehran, Iran*
[b] *Integrated Additive Manufacturing Center, Department Management and Production Engineering, Politecnico di Torino, Torino, Italy*

ARTICLE INFO

Article history:
Received 2 October 2022
Accepted 4 November 2022
Available online 9 November 2022

Keywords:
Low density steels
Substructure
Work hardening
Compression test
Dynamic recrystallization
Transformation

ABSTRACT

In the present work, the room temperature work hardening behavior and substructure evolution of Fe–17.5Mn–8.3Al–0.74C-0.14Si lightweight steel were investigated during compressive deformation. A series of compression tests were conducted under strain rates of $0.001s^{-1}$, $0.01s^{-1}$, and $0.1s^{-1}$. In addition, the compression tests were interrupted at strain levels of 0.25, 0.75, and 1.25 under the strain rate of $0.001s^{-1}$ to study the evolution of the substructure under compression. The starting and deformed microstructures were characterized through high-resolution electron back scatter diffraction (EBSD) technique. The obtained flow curves indicate the high capability of the experimented material for strain hardening. According to the microstructural observation, the outstanding mechanical properties are attributed to the capability of the alloy in cell structure formation and its progressive evolution to subgrains. Such extended dynamic recovery was followed by continuous dynamic recrystallization (CDRX) and deformation-induced ferrite transformation (DIFT) to accommodate the high amount of compressive strain (~2.5). These two mechanisms result in a final refined microstructure with ultrafine equiaxed grains which provides a great combination of strength and formability.
© 2022 The Authors. Published by Elsevier B.V. This is an open access article under the CC BY-NC-ND license (http://creativecommons.org/licenses/by-nc-nd/4.0/).

1. Introduction

In recent years, duplex lightweight steels have received extensive attention thanks to substantial lower density (reduction of up to 18%), due to the presence of higher aluminum content, as well as lower manufacturing costs in comparison with austenitic steels [1–3]. The dual-phase microstructures offer an incredible combination of strength and ductility, e.g., a high formability index over 50,000 MPa%, by exploiting both physical and mechanical properties of ferrite and austenite, simultaneously [4–6]. These features make the low-density steels suitable candidate for the manufacture of bodies in white (BIW) in the transportation industry [7,8]. This is because their low density reduces fuel

* Corresponding author.
E-mail address: habedi@iust.ac.ir (H.R. Abedi).
https://doi.org/10.1016/j.jmrt.2022.11.032
2238-7854/© 2022 The Authors. Published by Elsevier B.V. This is an open access article under the CC BY-NC-ND license (http://creativecommons.org/licenses/by-nc-nd/4.0/).

consumption while their high formability index enhances the crash performance and crashworthiness of the body structure. However, these alloys have a more complex microstructure compared to single-phase lightweight steels due to the mutual effect of the ferrite and austenite phases.

There are several strengthening mechanisms suggested to explain the continuous strain hardening and excellent mechanical properties of Fe–Mn–Al–C steels [9–14]. As lightweight steels contain more aluminum, leading to higher stacking fault energy (SFE) values (>50 mJ/m^2), the probability of twinning-induced plasticity (TWIP) and transformation-induced plasticity (TRIP) occurrences was found to be reduced [15–17]. Twin formation and $\gamma \rightarrow \alpha'$ transformation are mainly activated in the SFE ranges of 20–40 mJ/m^2 and 16–20 mJ/m^2, respectively [15]. The deformation twins and strain-induced martensite transformation would be inhibited as the aluminum content of Fe–Mn–Al–C alloys increases. In fact, the critical shear stress for twinning and the stability of austenite against the $\gamma \rightarrow \alpha'$ transformation increases with stacking fault energy. In this case, the governing deformation mechanism shifts from TRIP to TWIP to the formation of dislocation substructure in Fe–Mn–Al–C alloys. Therefore, the work hardening phenomena in the high SFE low-density steels can be explained by the intensified dislocation interactions [18]. Both ferrite and austenite phases have high stacking fault energy and are capable for the formation of dislocation cells and cellular structure owing to the wavy character of dislocation glide. The strengthening mechanisms have been also related to the substructure evolutions associated with planar glide such as Taylor lattice, Taylor lattice domain boundaries and crystallographic microbands. Planar glide is believed to be primarily caused by glide plane softening associated with short range ordering resulted from C–Mn octahedral clusters or shearable nano-sized κ-carbides [19–21]. It is therefore imperative to study the substructure development during deformation to tailor the microstructure properly and then achieve the desired mechanical properties. However, some other reports suggest that deformation mechanisms associated with austenite are not primarily governed by the SFE value. The austenite characteristics including grain size, preferred crystallographic orientation and morphology may also affect the stability of austenite and may trigger the tripping effect locally [14,22]. At this point, the optimal mechanical stability of austenite can explain the simultaneous operation of multiple deformation mechanisms.

Research on the room temperature formability of low-density steels has largely focused on tensile modes of deformation [9–13,18–20,22]. As an example, Abedi et al. [18] examined the effects of substructure development on the room temperature deformation behavior of Fe–Mn–Al–C–Si lightweight steel using tensile testing method. They demonstrated that the significant strain hardening capability of the studied steel was attributed to the progressive evolution of cell structures into subgrains during straining. Subgrain evolution continued until fracture (but slowed down after size stabilization), indicating the importance of such mechanisms for strain accommodation during room temperature tensile deformation. Also, the continuous subgrain refinement could lead to the nano-size partitioning of the austenite (~530 nm) and ferrite (~500 nm) grains, resulting in excellent mechanical properties. Furthermore, tailoring the microstructure using heat treatment has been of interest since high Al and C promote the formation of κ-carbides [23–25]. Nevertheless, there are a few reports in the literature focusing on the compressive formability of the lightweight steels at room temperature. Li et al. [26] assessed the compressive deformation behavior of micro-alloyed Fe–Mn–Al–C low-density steel aged at different temperatures. It was found that high strain rate had a prominent effect on strain hardening behavior, which was due to the enhanced interaction of mobile dislocations and distributed κ-carbide within austenite. In the case of higher strain rates, the obtained compressive flow curves revealed continuous hardening that was followed by shear fracture. Yet, the investigation of the microstructure without the presence of κ-carbide and its impacts on the room temperature compressive formability of such alloys have been overlooked. No study has been conducted to investigate the relationship between compressive mechanical performances, particularly work hardening behavior, and substructure development of low-density steel. In light of this knowledge gap, the goal of the present work is to examine the compressive deformation behavior as well as substructural development of a low-density κ-carbide free steel at the ambient temperature.

2. Experimental procedure

2.1. *Material specification*

The chemical composition of the low-density steel experimented in this work is summarized in Table 1. This alloy is expected to have a lower density than fully austenitic structures because of the presence of a high amount of Al. The apparent density of 6.8 gr/cm^3 was determined for the specified steel with a properly calibrated densitometer (Mettler-Toledo XP205), which represents a remarkable reduction (~16%). Moreover, the austenite stacking fault energy (SFE) value of 85–90 mJ/m^2 was measured using the sub-regular solution thermodynamic model proposed by Saeed-Akbari et al. [27], considering effects of alloying elements of Mn, C, and Al as well as initial grain size. As a result, this value is significantly greater than that of for activation of deformation twinning (20–40 mJ/m^2) or austenite to martensite dynamic transformation (16–20 mJ/m^2) [15].

The material was prepared by atmosphere-controlled induction melting followed by electroslag re-melting. After homogenizing the cast material at 1200 °C for 1 h, the alloy was hot rolled in the temperature range of from 1150 °C (start temperature) to 900 °C (finish temperature), then air cooled. As this lightweight steel can exhibit a duplex structure containing a predominant austenite phase over a wide range of

Table 1 – The chemical composition of the experimented alloy.

Element	Mn	Al	C	Si	Fe
wt.%	17.5	8.3	0.74	0.14	Bal.

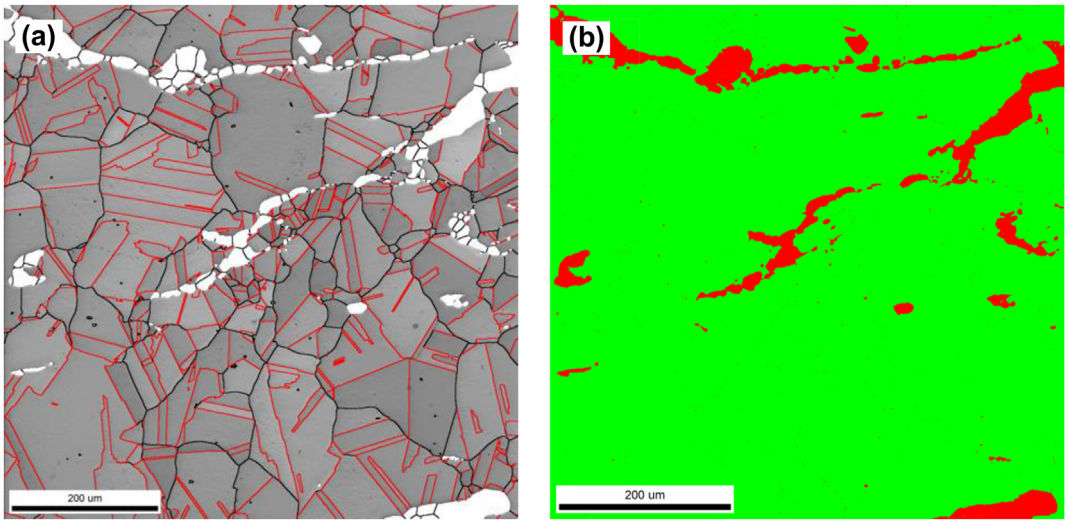

Fig. 1 – (a) Image quality and (b) phase map of the initial duplex microstructure of the experimented low-density steel. Red areas correspond to the ferrite phase.

temperatures [18], a short-time annealing procedure at 1100 °C for 10 min was carried out on the hot rolled material to create a dilute solid solution dual phase ($\gamma+\alpha$) microstructure. The obtained as-annealed microstructure of the alloy with an average grain size of ~28 μm along with its corresponding phase map as a duplex structure are illustrated in Fig. 1. As it can be seen, a high fraction of annealing twins is evident in the initial γ-austenite grains (red boundaries in Fig. 1a) along with the α-ferrite phase (red regions shown in Fig. 1b). The austenite and ferrite fractions are approximately 90% and 10%, respectively.

2.2. *Mechanical tests*

For the compressive behavior study of the alloy, the as-annealed cylindrical samples with dimensions of Φ8 mm * 12 mm were prepared based on the ASTM E9 standard [28]. These samples were subjected to room temperature compression tests under various strain rates of 0.001s^{-1}, 0.01s^{-1}, and 0.1s^{-1}. To ensure repeatability and reproducibility, each test conducted under specified conditions was repeated three times and the mean values were reported. It is worth mentioning that compression tests are generally conducted down to true strains of 0.5–0.6 to prevent barrelling effects caused by excessive friction between the anvil and specimen surfaces observed at higher straining. As a result of the friction effect, there is an additional stress in the overall estimation of flow stress along with the transverse stress that is responsible for surface cracking. In this case, however, an unconventional approach was adopted, in which the tests were conducted without any particular lubricant until a true strain of 2.5 at the strain rate of 0.001 s^{-1}, in order to evaluate the capability of the alloy in strain accommodation and compressive formability at room temperature. The results were reported as true strain–true strain ($\sigma-\varepsilon$) and work hardening rate–true strain ($d\sigma/d\varepsilon-\varepsilon$) plots. In addition, interrupted compression tests were performed at strain levels of 0.25, 0.75, and 1.25 under the strain rate of 0.001s^{-1} to investigate the substructure evolution during the compression test.

2.3. *Microstructure examination*

To accurately examine the substructure development, the microstructures of samples compressed down to various strain levels of 0.25, 0.75 and 1.25 were explored through high resolution electron back scatter diffraction (EBSD). For this purpose, a Zeiss LEO 1530 FEG SEM operated at 20 kV was utilized to acquire the EBSD data, following mechanical polishing and electropolishing at room temperature in CH3COOH (92%) and HClO4 (8%) solutions under a voltage of 32 V. The instrument had an automatic EBSD attachment from HKL Technology (now Oxford Instruments). HKL Channel 5 and Aztec software were used for data acquisition and post-processing, including a modified Kuwahara filter for averaging origination data.

3. Results and discussion

3.1. *Hardening behavior*

Fig. 2 represents the true stress vs. true strain ($\sigma-\varepsilon$) and work hardening rate vs. true strain ($d\sigma/d\varepsilon-\varepsilon$) curves of the experimented alloy during room temperature compression tests under the strain rates of 0.001 s^{-1}, 0.01 s^{-1}, and 0.1 s^{-1}. It is found that there is a maximum flow stress followed by a noticeable softening in the present study which is unlike the typical room temperature compressive flow behavior observed for most other materials. In general, various alloys exhibit progressive increase in room temperature compressive flow stress with strain increased. However, in the present alloy, it is possible to observe continuous flow softening as well as superformability at room temperature, which is an exceptional characteristic for advanced high strength lightweight steels. This is despite the fact that such softening is

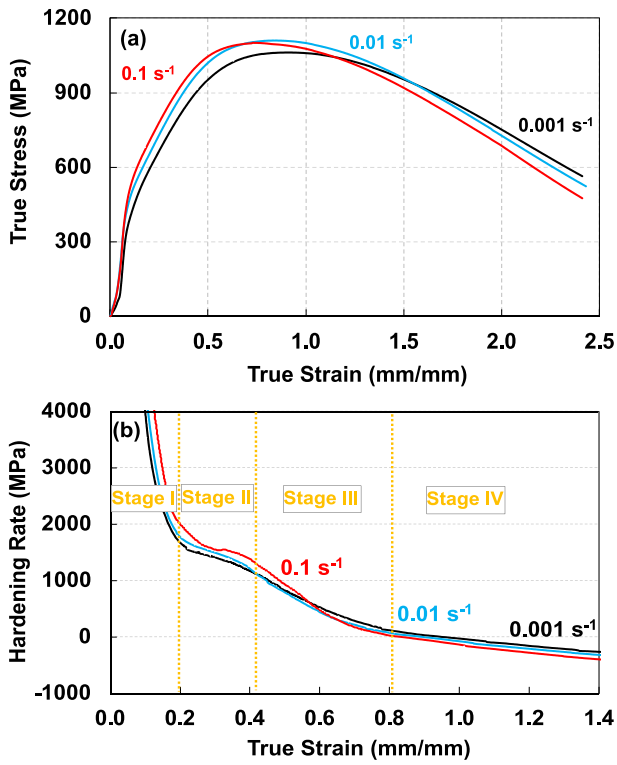

Fig. 2 – (a) The true stress–strain curves of the studied steel under the various strain rates and (b) the corresponding work hardening rate in terms of true strain.

normally expected to take place at higher temperatures, exceeding 600 °C [29–31], at which thermally activated processes like dynamic recrystallization (DRX) are likely occur. It can be also observed that strain rates directly influence the yield stress so that a higher yield stress is obtained at the higher strain rate. To compare yield points quantitatively, $\sigma_{0.2}$ values were measured based on the true stress–strain curves and summarized in Table 2 ($\sigma_{0.2}$ corresponds to the 0.2% proof stress). As can be seen in Table 2, the yield stress values under the strain rates of 0.001 s^{-1}, 0.01 s^{-1}, and 0.1 s^{-1} are 309 MPa, 351 MPa, and 393 MPa, respectively. The corresponding peak stress values are also 1061 MPa, 1109 MPa, and 1100 MPa, respectively, which indicate the positive effect of strain rate on yield and peak stresses. However, the flow behavior of the material seems to be relatively strain rate insensitive. The room temperature strain rate sensitivity of high strength steels (and the majority of engineering materials) in quasi-static regime relatively equals to zero and may be increased to positive values under higher strain rate domains as was reported by Wu et al. [32] in the case of Fe–28Mn–10Al–1.2C low-density steel alloy. Another relevant observation to consider is the more pronounced softening in the sample deformed under the higher strain rate which may suggest the high capability of the experimented material for restoration and rearrangement of the dislocation substructure.

According to Fig. 2b, it is evident that the work hardening rate ($d\sigma/d\varepsilon$) decreases continuously with an increase in strain and pass over the negative range which is similar to the dynamic recovery regime observed in high-SFE FCC metals. In

Table 2 – Room temperature compressive properties of the studied alloy.

Strain rate (s^{-1})	0.001	0.01	0.1
$\sigma_{0.2}$ (MPa)	309.3 ± 5.6	351.2 ± 4.8	393.9 ± 5.1
σ_{max} (MPa)	1061.5 ± 4.3	1109.7 ± 3.8	1100.8 ± 4.1
Transition strain (%) (Stage I to II)	19.6 ± 0.2	18.6 ± 0.3	17.1 ± 0.3
Transition strain (%) (Stage II to III)	40.7 ± 0.3	41.7 ± 0.2	38.2 ± 0.2

this case, the work hardening behavior can be classified into four distinct regions based on various descending slopes observed in the curves. The initial sudden drop in work hardening rate associated with the elastoplastic transition is defined as stage (I), during which the dislocation mean free path is high (dislocation density is low) enough to prevent tangling. Following the elastoplastic transition, stage (II) is characterized by an almost constant work hardening rate up to a true strain of about 0.4. This behavior is entirely different from the work hardening rate changes observed for the same alloy in the tensile mode where rapid hardening occurs in stage (II) [18]. In this stage, the strain hardening coefficient value varies between G/40–G/60, where G is the alloy shear modulus, G = 70 GPa [33]. These values are less than those found for Fe–Mn–C alloys (laying in the range of G/20–G/40 [18,34–36]). These observations generally point out that the effect of deformation mode on the capability of substructure development in experimented steel is prominent which can have significant influences on the mechanical properties such as formability. Stage (III) is identified as a continuous decline in the work hardening rate with an increase in strain, which finally passes over to the negative range in stage (IV). The true strains of about 0.8 was recorded as transition strain in the present case. The negative hardening rate, i.e. the occurrence of softening, in stage (IV) indicates that the experimented material can accommodate large amount of compressive applied strains. The final stage of hardening has not been observed for the same alloy in the tensile mode [18,37]. This can be due to the inherent limitations of tensile testing in the attained amount of plastic strain resulting from the occurrence of necking phenomenon.

It is worth noting that the transition strain level from stage (I) to stage (II) appears earlier in the specimen compressed under the strain rate of 0.1s^{-1} (at the true strain of ~0.171, see Table 2) as compared to the other samples deformed at the lower strain rates. Generally, the created moving dislocations during the initial stage of deformation are tangled at the end of stage I and are capable to be rearranged into dislocation cell substructures with further straining. Therefore, the faster decay of the work hardening rate observed in the stage (I) of the sample deformed at the higher strain rates could be associated with a more rapid tangling and subsequent rearrangement of the dislocations. Generally, a variety of factors have been reported in this respect, including initial large grain size, low dislocation density, and rapid dislocation movement [38]. Larger grain sizes allow dislocations to move more freely, and the lower dislocation density the less interaction between dislocations. Given the same initial microstructure under all

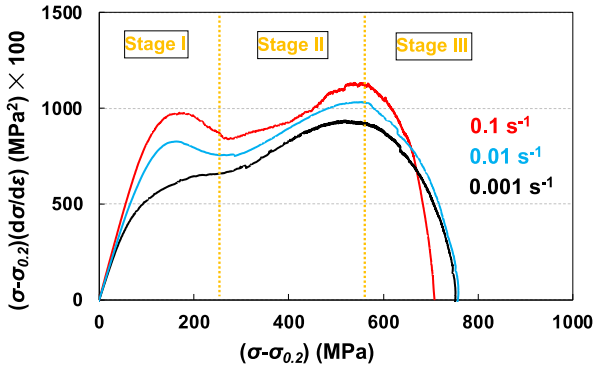

Fig. 3 – The (σ-$\sigma_{0.2}$) (dσ/dε) vs. (σ-$\sigma_{0.2}$) curve for the studied steel under the various strain rates.

deformation conditions, these two factors cannot be the reason for the faster decline of the work hardening rate in the sample deformed at the higher strain rate. In fact, to accommodate the overall applied strain under the higher strain rate, the dislocations might move faster which can lead to the earlier tangling, and rearrangement of the dislocations. A nearly constant work hardening rate is obtained during stage (II) for the sample compressed under the various strain rates. In stage (III), it is obvious that the work hardening rate reduction is faster in the case of higher applied strain rate, indicating the high capability of material for strain accommodation and dislocation restoration which can positively affect the compressive formability of the material. For a better comparison of the work hardening rates under different strain rates, (σ-$\sigma_{0.2}$) (dσ/dε) was plotted in terms of (σ-$\sigma_{0.2}$) as shown in Fig. 3. It has been reported that the relationship between (σ-$\sigma_{0.2}$) (dσ/dε) and (σ-$\sigma_{0.2}$) is equivalent to that of between dislocation storage rate (dρ/dε) and dislocation density ($\rho^{1/2}$), where ρ is total dislocation density [39].

The initial slope in the (σ-$\sigma_{0.2}$) (dσ/dε)–(σ-$\sigma_{0.2}$) curve is mainly influenced by grain size. Given the same initial microstructure for all conditions, the same slopes are achieved at the beginning of the deformation. With the further

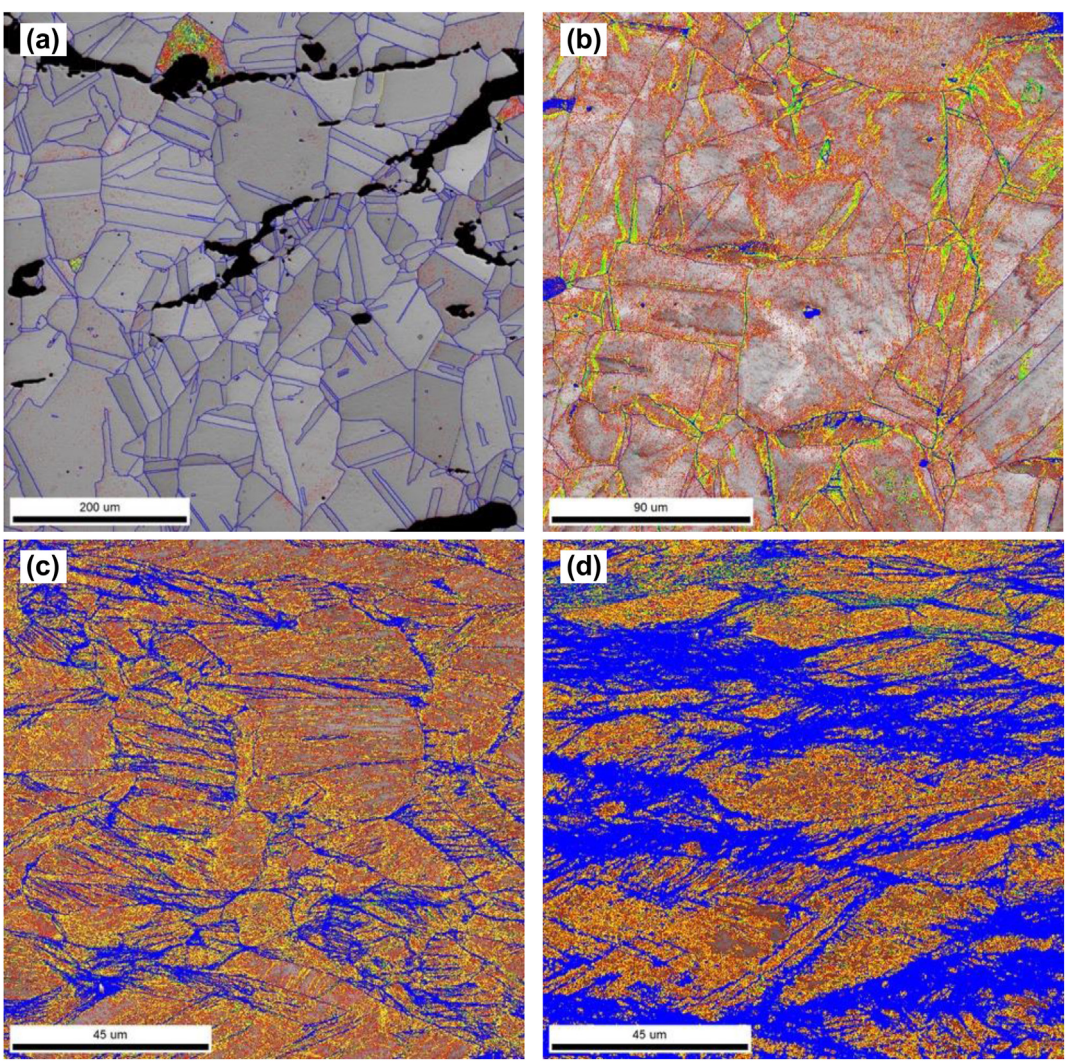

Fig. 4 – Boundary maps of (a) the initial microstructure and deformed after strains of (b) 0.25, (c) 0.75, and (d) 1.25. The respective green, red, yellow, and blue colors display the misorientation angles of 0.7°<θ<2°, 2°<θ<5°, 5°<θ<15°, and θ>15°.

application of deformation, however, the higher strain rate leads to the more rapid formation of dislocation forests, causing more rapid increase in dislocation storage rate as can be seen in Fig. 3. In this case, the dislocation storage rate reaches the first peak, followed by an initial drop in the end of stage (I) of hardening that could be the reason for earlier occurrence of stage (II). In contrast, a gradual progressive increase of the dislocation storage rate can be seen in stage (I) for the sample compressed under the strain rate of 0.001 s^{-1}, showing the capability of the alloy to accommodate the applied strain at the lower strain rate. The observed increasing trend of the dislocation storage rate in stage (II) is almost same for all samples, while it is different in stage (III). In stage (III), the dislocation storage rate tends to decline fast. The reduction is more rapid in the sample deformed under the strain rate of 0.1 s^{-1} than the strain rate of 0.001 s^{-1}, supporting the idea of high ability for microstructure restoration and compressive formability even under the high strain rates.

3.2. *Substructure development*

To investigate the substructure development (i.e., subgrain formation, refinement, coalescence and probable transformation) during compression deformation, a precise examination of the microstructure was conducted on the sample deformed at the strain rate of 0.001 s^{-1}. This case was selected since the probable microstructural changes would be more apparent. The deformed microstructures at various levels of strains were analyzed and compared with the initial microstructure. Fig. 4 represents the austenite boundary maps attained from high resolution EBSD for the experimented alloy in the states of as annealed and compressed down to the strain levels of 0.25, 0.75, and 1.25. It should be noted that the strains of 0.25, 0.75, and 1.25 were of interest as they correlate with the respective stages (II), (III), (IV) of hardening as shown in Fig. 2b. According to Fig. 4, it is apparent that the subgrains within austenite grains evolve continuously and dynamically. The austenite grains subdivide into several sub grains during the straining process. The yellow, red, green, and blue colors display the misorientation angles of $0.7^\circ < \theta < 2^\circ$, $2^\circ < \theta < 5^\circ$, $5^\circ < \theta < 15^\circ$, and $\theta > 15^\circ$, respectively. In the as-annealed microstructure, the misorientation angles are mostly larger than 15°, corresponding to high angle grain boundaries (HAGB) (blue lines in Fig. 4a). Besides, the presence of the parallel bands within the austenite grains is indicative of the high frequency of annealing twins in the initial microstructure. As a result of compressive deformation at room temperature, austenite grains are composed of a variety of subboundaries with misorientation angles of <15°. The results demonstrate that the annealing twins seem to be vanished by

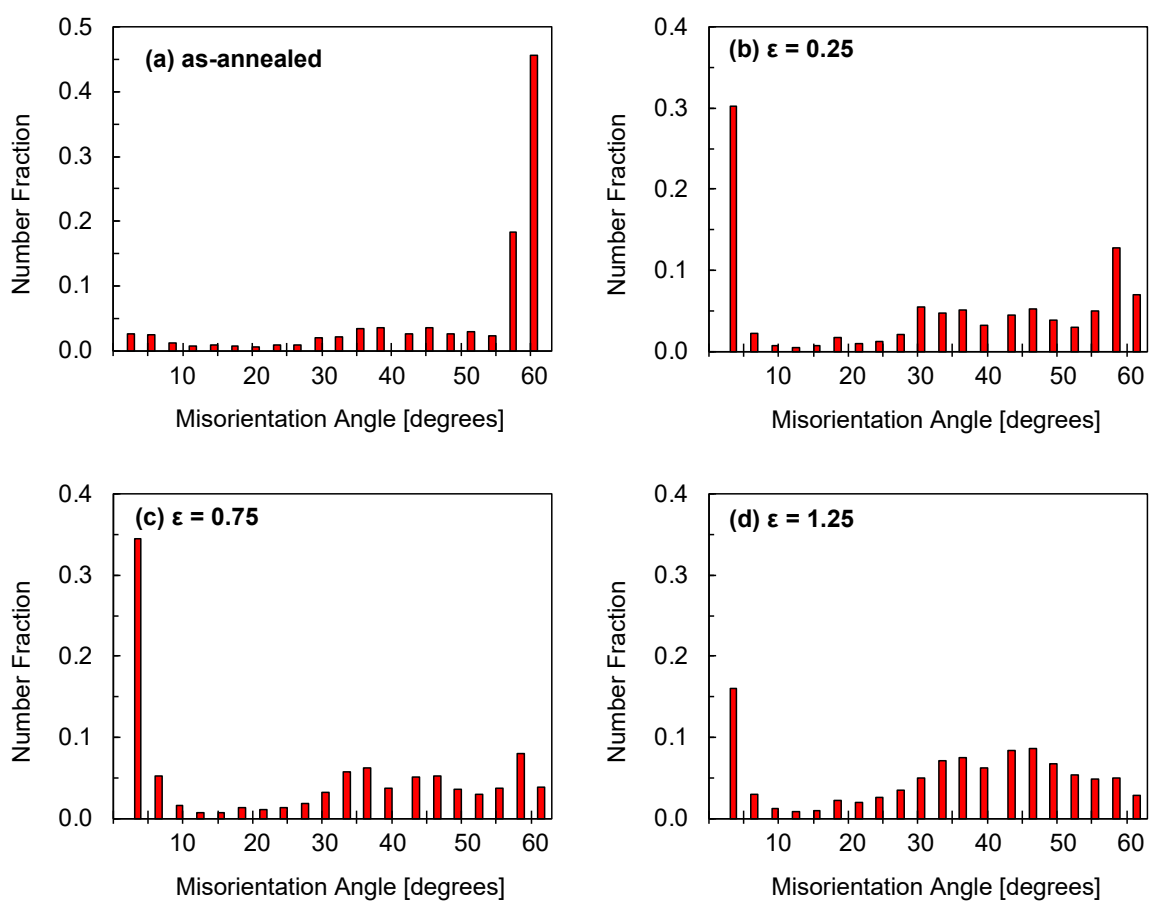

Fig. 5 – Misorientation angle distributions of (a) the initial microstructure and the samples compressed down to the strain levels of (b) 0.25, (c) 0.75, and (d) 1.25.

applying a small strain of 0.25, while subgrain boundaries with low misorientation angles start to form in the original austenite grains.

As a result of further straining, subgrains with low angle grain boundaries (LAGB) become more frequent (Fig. 4c). The cell walls (now known as subgrain boundaries) exhibit different misorientations that allow further sub-classification. The network of cell structure in the areas nearer the grain boundaries is denser, where the sub-boundaries have greater misorientation angles in the range of $2^\circ < \theta < 5^\circ$ and $5^\circ < \theta < 15^\circ$ compared to the interior grains ($0.7^\circ < \theta < 2^\circ$). By inducing more strain, LAGBs are transformed into HAGBs (Fig. 4d) and fine grains surrounded by HAGBs are produced within and along the grain boundaries of coarse austenite. The misorientation angle distributions between neighboring grains/subgrains are provided in Fig. 5 for a more quantitative analysis of substructure development. It should be noted that boundaries with the misorientation angles of $0.7^\circ < \theta < 2^\circ$ were excluded in this measurement. In the as-annealed condition (Fig. 5a), the majority of misorientations holds the angles of between 15° and 60° in which the highest frequency can be observed around the angle of 60°. This can confirm the existence of annealing twins in the initial microstructure (Fig. 1a) as the Σ3 twin boundaries are identified as 60° rotation around a ⟨111⟩ axis. As the deformation progresses, however, the frequency of the annealing twins decreases. In fact, their misorientation axis/angles diverge from the perfect coincidence during straining, resulting in a significant reduction of

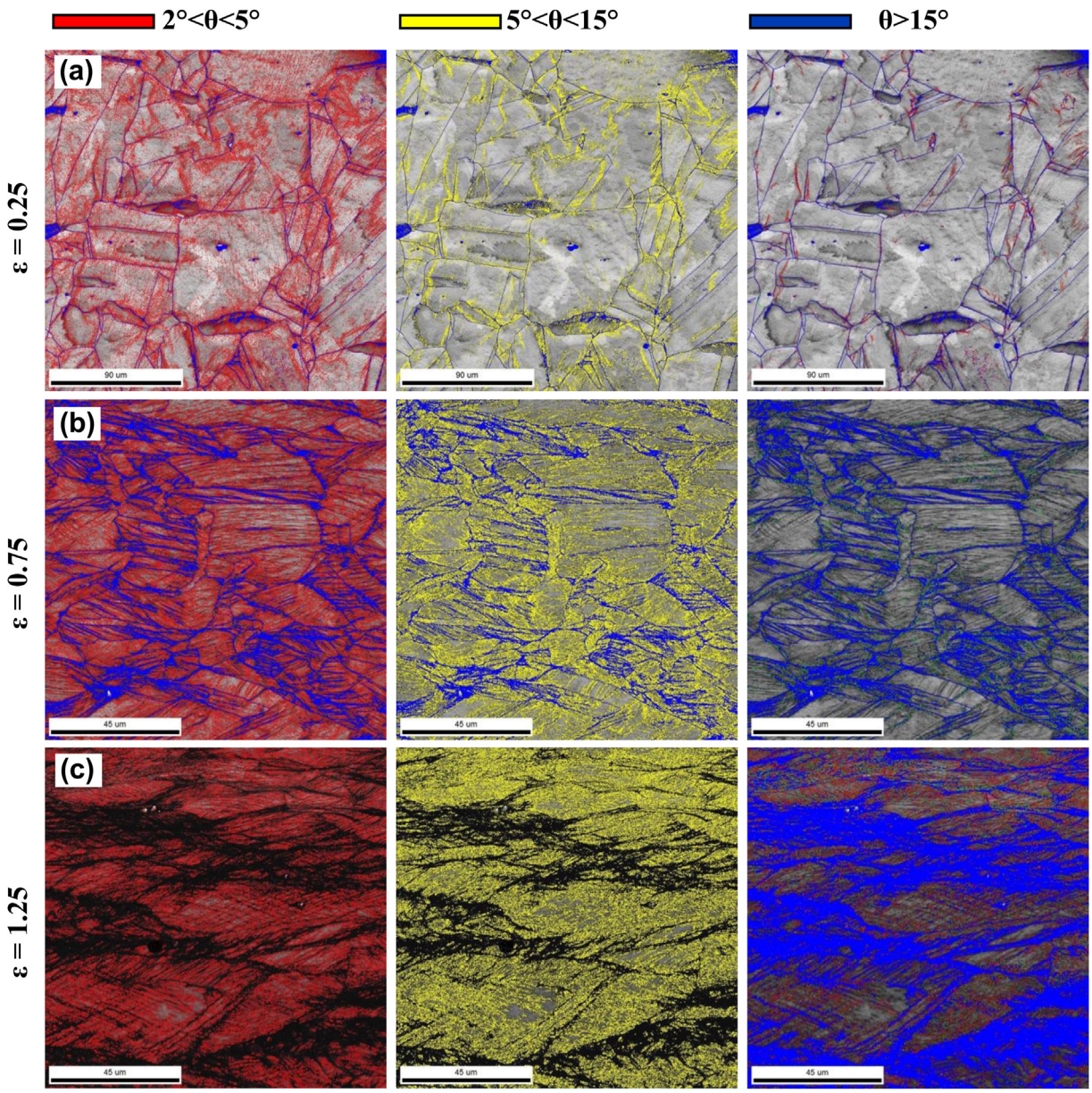

Fig. 6 – A detail illustration of the boundary maps of the subgrains in the sample deformed under the strain rate of 0.001 s^{-1} after the strain levels of (a) 0.25, (b) 0.75, and (c) 1.25. The respective red, yellow, and blue colors display the misorientation angles of $2^\circ<\theta<5^\circ$, $5^\circ<\theta<15^\circ$, and $\theta>15^\circ$.

the annealing twin number (Fig. 5b, c, d) as can be seen in the microstructures from Fig. 4b, c, d. Meanwhile, the frequency of sub-boundaries increases and LAGBs with a number fraction of 30–40% are observed within the coarse austenite grains at the interrupted strains of 0.25 and 0.75. When higher strains are imposed, misorientation angle changes become different from those observed with interrupted strains of 0.25 and 0.75. The misorientation angles of LAGBs gradually increase by continuing deformation, so that most of them are shifted to the higher angles ($\theta > 15^\circ$).

According to the described phenomena, the microstructural evolution may have been accompanied by DRX, which can explain the occurrence of softening in the flow curves shown in Fig. 2a. It is actually identified these intensified substructure developments and the presence of incomplete grain boundaries as characteristics of continuous dynamic recrystallization (CDRX). A similar mechanism has previously been observed with the same alloy during room temperature tensile deformation [18]. The main difference is that in compressive mode of deformation the extent of substructure development and subsequent recrystallization is higher. This can be discussed relying on the higher amount of imposed strain, and the different compressive flow pattern with tensile one which provide proper condition for intensified dislocation tangling for subsequent re-arrangement.

In previous researches, the occurrence of dynamic recovery and substructure development at room temperature, has been discussed relying on the high stacking fault energy of lightweight steels and the capability for cell-structure formation [40–43]. In this respect, Akbarian et al. [40] have reported that such extended dynamic recovery ends in continuous dynamic recrystallization at room temperature during multiaxial forging (MAF) of Fe–29.1Mn–0.039C-2.4Al–0.3Si alloy. In the present case, the compressive mode of deformation and the high amount of imposed strain are similar to the condition experienced in the course of MAF, as a well-known sever plastic deformation method, so the occurrence of CDRX could be explained by the evolution of the substructure during room temperature deformation.

Generally, in twinning-induced plasticity steels with low stacking fault energy, which can be difficult to form cell structures, the diffused dislocation arrangements such as tangles or other more random structures may still be observed after larger strains [21]. As stacking fault energy reaches the medium range, the substructure formation and refinement involved in planar and wavy patterns tend to lead to the early stages of hardening [12,13]. This experiment considers the progressive and effective orderly formation of the subgrains (LAGB) as a unique microstructural characteristic of the studied alloy in response to room temperature compressive straining. This intensified substructure development is followed by recrystallization, and it is believed that this mechanism is responsible for the observed high capability of the material for strain hardening/softening under room temperature compressive deformation.

Fig. 6 represents a more detailed view of boundary maps for a better understanding of substructure development of deformed samples. The respective red, yellow, and blue colors represent the misorientation angles of $2^\circ < \theta < 5^\circ$, $5^\circ < \theta < 15^\circ$, and $\theta > 15^\circ$. The gradual formation of cell structure within the coarse austenite grains followed by a progressive transition into the subgrains holding sharp sub-boundaries can be clearly seen in the developed microstructures. In the deformed microstructure at the interrupted strain of 0.25 (Fig. 6a), a high fraction of incomplete sub-boundaries, holding misorientation angles of $2^\circ < \theta < 5^\circ$ and $5^\circ < \theta < 15^\circ$ (red and yellow colors, respectively), is indicative of the dislocations cell structure formation. Near the prior grain boundaries, the network of the cell structure is denser with a greater misorientation angle of sub-boundaries than the interior grains. The misorientation of low angle boundaries are gradually increased during deformation as a result of more dislocation formation and absorption into the pre-existing sub boundaries (Fig. 6b). A high amount of HAGBs (blue lines) with a wide distribution along with the deformed grains can be seen at the true strain of 0.75. This means that recrystallized grains have begun to form partially, corresponding to the stage (III) of hardening where the work hardening rate tends to decrease more rapidly compared to stage (II) and pass over to the negative range. Besides increasing of HAGB, an appreciable subgrain refinement takes place by inducing strain.

Considering the subgrain size distribution histograms given in Fig. 7, it can be inferred that an almost normal distribution of the subgrains has been achieved during the

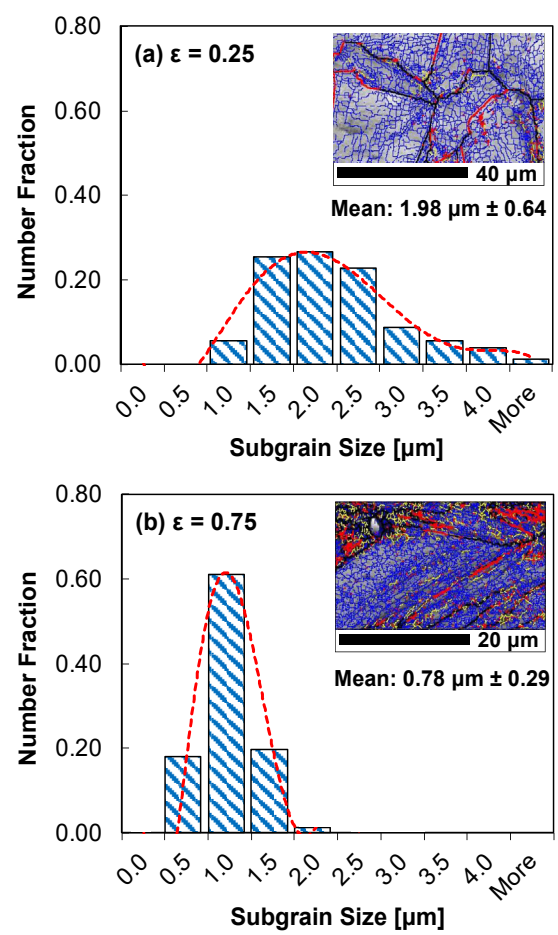

Fig. 7 – Subgrain size distributions of the samples compressed down to the strain levels of (a) 0.25 and (b) 0.75.

compression deformation. These substructure evolutions and histograms show the great potential of the studied alloy in developing a well-refined uniform subgrain structure within the prior austenite grains. In addition, the average subgrain size shifts to smaller values with a narrower distribution of subgrain size as deformation proceeds. The average subgrain size reduces from 1.98 μm at the true strain of 0.25–0.78 μm at the true strain of 0.75 (misorientation angle threshold has been considered to be 0.7°). The LAGBs convert to HAGBs as a result of increased strain-induced misorientation angles. This results in a high percentage of HAGB being produced (blue color in Fig. 6c) in interrupted true strains of 1.25, indicating a large percentage of recrystallized grains. The capability of grain refinement is correlated with substructure size stabilization. The widespread distribution of the recrystallized grains in the microstructure corresponds to stage (IV) of work hardening where softening overcomes hardening as seen in Fig. 2b. Accordingly, slip activation through wavy movement of dislocations is the primary mean of accommodating strain in austenite. In fact, the wavy character of dislocation movement and high dislocation motility provide a proper condition for the formation of dislocation cells and subgrains followed by the occurrence of CDRX. This well justify the observed softening behavior in corresponding flow curves at room temperature.

The phase map of the microstructures at the mentioned interrupted true strains are shown in Fig. 8. According to the results, during compressive straining, ferrite phase fractions increase in the deformed microstructures. This may be due to dynamic transformation of the prior austenite to ferrite in response to the high amount of imposed strain. As indicated by black dashed rectangle in Fig. 8c, ultrafine ferrite and austenite grains can be detected in selected areas of the microstructure. This means that straining leads to the formation of fresh ferrite grains from the recrystallized austenite phase. Therefore, it can be inferred that the new ultrafine austenite and ferrite grains are created through the occurrence of dynamic recrystallization and dynamic transformation, respectively. The deformation-induced ferrite transformation (DIFT) has been identified as the most effective mechanism contributing to grain refinement which can be related to an increase of both austenite free energy and

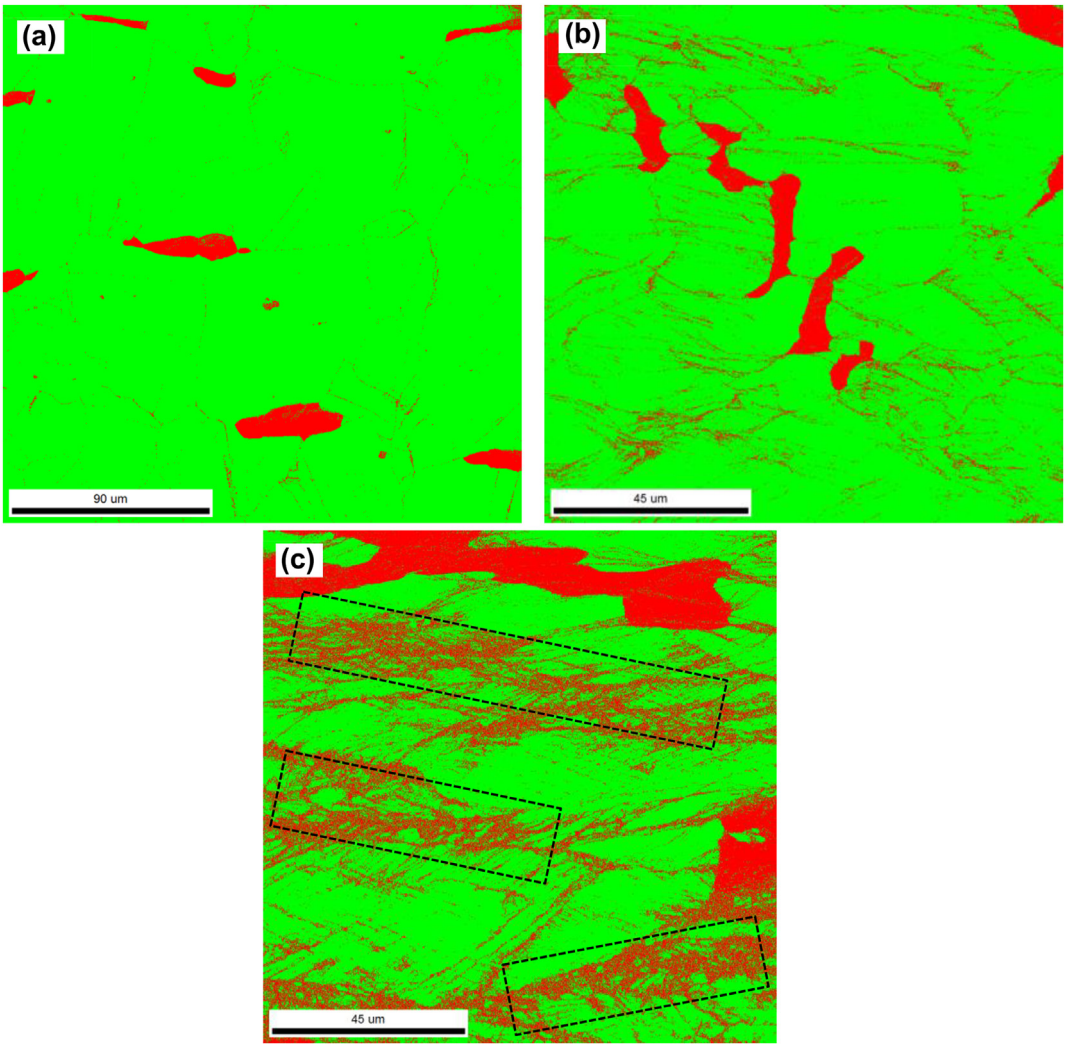

Fig. 8 – Phase maps of the microstructures after the strains of (a) 0.25, (b) 0.75, and (c) 1.25 indicating the formation of fresh ferrite grains within the austenite, and fine austenite grains within the prior ferrite during compression.

Table 3 – Comparison of the deformation mechanism and mechanical properties of duplex Fe–Mn–Al–C steel ($\alpha + \gamma$).

Chemical composition	Deformation mode	Dominant deformation mechanisms	Rapid hardening	Yield stress (MPa)	Peak stress (MPa)	Ref.
Fe–18Mn–8Al–0.7C-0.1Si	Tension	Wavy glide (subgrain formation) + Twinning	Yes	~400	~1200	[18]
Fe–18Mn–8Al–0.7C-0.1Si	Compression	Wavy glide (subgrain formation)	No	~310	~1100	This work

nucleation site density caused by deformation applied. The details of strain induced ferrite formation and austenite stability have been thoroughly described in previous works [44–46]. Interestingly, the formation of new fine austenite grains can be traced within the prior ferrite grains (Fig. 8c) indicating the occurrence of bidirectional transformation which has been previously reported in the case of low-density steels at warm temperature regime (~500 °C) [47]. Generally, each of deformation variables including strain, strain rate, temperature or deformation mode could influence $\gamma \rightarrow \alpha$ transformation [48]. Chemical free energy and deformation stored energy make up the total driving force under deformation conditions. As a result of this excess energy, austenite can transform into ferrite and vice versa. In the present case, according to the high imposed strain, driving force of the transformation has been provided. Accordingly, the strain-induced austenite to ferrite transformation can be considered as another strain compensation mechanism in addition to recrystallization to explain the observed flow softening at the room temperature deformation (Fig. 2a).

As a final point, the mechanical properties obtained from the current work and the results obtained from the previous study on the tensile behavior of the same alloy are summarized in Table 3. Deformation mechanisms and various parameters such as yield stress and peak stress, have been derived. This experimental steel shows excellent mechanical properties such as compressive yield stress of 310 MPa and peak stress of 1100 MPa. Different deformation mechanisms, including twinning, wavy/planar glide, slip band refinement and crystallographic micro-banding, can be responsible for the outstanding mechanical properties of duplex low-density steels. In the present case, the unique characteristics are largely due to rapid dislocation multiplication and subsequent interactions that result in progressive subgrain evolution (formation, refinement, and possibly rotation/coalescence) within the austenite grains. The substructure development was followed by continuous recrystallization and accompanied by the bi-directional transformation of austenite to ferrite. As compared to the tension mode, the yield and peak stress values appear to be slightly lower in the compression mode. To have a better comparison between tension and compression modes, subgrain size changes at various true strains are plotted in Fig. 9a. In addition, the corresponding true stress values are replotted in Fig. 9b. As can be seen, the subgrain size reduction for tension mode is more rapid than compression mode. At true strain of ~0.25, a smaller subgrain size has been attained in the compressive deformation mode (Fig. 9a) while higher true stress has been experienced in the tensile mode (Fig. 9b). On the other hand, at the nearly same subgrain size values (at the respective true strains of 0.4 and 0.75 for tension and compression deformation modes), approximately same stress levels have been achieved. In this case, the significant point is that obtaining the same subgrain size takes place at a higher true strain in compression. These findings reveal that changing the load direction and the resultant compressive flow pattern can directly influence the quality of substructural development in experimented alloy.

In this respect, the dislocation mean-free path, the planar/wavy character of dislocation glide and in general dislocation maneuverability, should be compared (between tensile and compression modes) in correlation with developed texture components. These characteristics directly influence on the

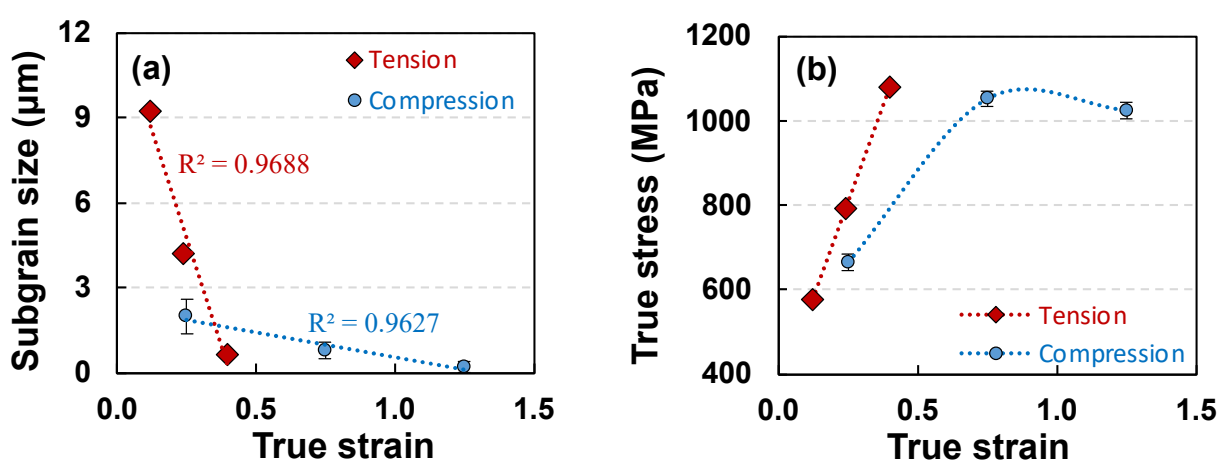

Fig. 9 – (a) Subgrain size changes with true strain and (b) the corresponding true stress plots for duplex Fe–Mn–Al–C steel ($\alpha + \gamma$) in two different deformation modes (The tensile results are educed from Ref. [18]).

capability of dislocation tangling and rearrangement, subgrain rotation and coalescence, dislocation dissociation and absorption to the high angle boundaries, and indirectly dictate the capability of the material for strain accommodation. This can be considered as the subject of future works.

4. Conclusions

The involved hardening mechanisms during compressive room temperature deformation of a duplex ($\alpha + \gamma$) low density steel were precisely studied emphasizing on the quantitative and qualitative characterization of substructure development. The following conclusion were drawn:

- The compressive flow curves showed four distinct work hardening rate stages. They were surprisingly accompanied with appreciable softening up to high imposed strain instead of the conventionally expected continuous strain hardening observed in compression behavior of most alloys that has been related to the substructure development during straining.
- The continuous and progressive formation of the subgrains within the microstructure was clearly recognized using EBSD. The network of the cell structure at the vicinity of the grain boundaries was denser and the sub-boundaries possess higher misorientation angles, ($2^\circ < \theta < 15^\circ$) compared to the interior grains ($0.7^\circ < \theta < 2^\circ$). The measurements indicated an appreciable subgrain refinement, e.g., the average subgrain size reduces from 1.98 μm at the true strain of 0.25–0.78 μm at the true strain of 0.75.
- After size stabilization, the subgrain evolution slowed down until the CDRX mechanism is completed.
- The subgrain evolution continued up to the higher applied strain but slowed down after size stabilization, in the meantime, the CDRX mechanism was completed. Accordingly, such mechanism appears to play an influential role in strain accommodation during room-temperature compressive deformation, explaining the observed softening and high formability.
- In addition, strain-induced austenite to ferrite transformation was also identified during straining in the microstructure that can be considered as another strain compensation mechanism to explain the observed flow softening at the room temperature deformation.

Declaration of Competing Interest

The authors declare that they have no known competing financial interests or personal relationships that could have appeared to influence the work reported in this paper.

REFERENCES

[1] Raabe D, Springer H, Gutierrez-Urrutia I, Roters F, Bausch M, Seol JB, Koyama M, Choi PP, Tsuzaki K. Alloy design, combinatorial synthesis, and microstructure–property relations for low-density Fe–Mn–Al–C austenitic steels. J Occup Med 2014;66:1845–56. https://doi.org/10.1007/s11837-014-1032-x.

[2] Chen S, Rana R, Haldar A, Ray RK. Current state of Fe–Mn–Al–C low density steels. Prog Mater Sci 2017;89:345–91. https://doi.org/10.1016/j.pmatsci.2017.05.002.

[3] Song H, Yoo J, Kim SH, Sohn SS, Koo M, Kim NJ, Lee S. Novel ultra-high-strength Cu-containing medium-Mn duplex lightweight steels. Acta Mater 2017;135:215–25. https://doi.org/10.1016/j.actamat.2017.06.035.

[4] Suh DW, Kim NJ. Low-density steels. Scripta Mater 2013;68:337–8. https://doi.org/10.1016/j.scriptamat.2012.11.037.

[5] Rana R. Low-density steels. J Occup Med 2014;66:1730–3. https://doi.org/10.1007/s11837-014-1137-2.

[6] Hu S, Zheng Z, Yang W, Yang H. Fe–Mn–C–Al low-density steel for structural materials: a review of alloying, heat treatment, microstructure, and mechanical properties. Steel Res Int 2022;93:2200191. https://doi.org/10.1002/srin.202200191.

[7] Kim H, Suh DW, Kim NJ. Fe–Al–Mn–C lightweight structural alloys: a review on the microstructures and mechanical properties. Sci Technol Adv Mater 2013;14:014205. https://doi.org/10.1088/1468-6996/14/1/014205.

[8] Rana R, Liu C, Ray RK. Low-density low-carbon Fe–Al ferritic steels. Scripta Mater 2013;68:354–9. https://doi.org/10.1016/j.scriptamat.2012.10.004.

[9] Hwang SW, Ji JH, Lee EG, Park KT. Tensile deformation of a duplex Fe–20Mn–9Al–0.6C steel having the reduced specific weight. Mater Sci Eng, A 2011;528:5196–203. https://doi.org/10.1016/j.msea.2011.03.045.

[10] Ha MC, Koo JM, Lee JK, Hwang SW, Park KT. Tensile deformation of a low-density Fe–27Mn–12Al–0.8C duplex steel in association with ordered phases at ambient temperature. Mater Sci Eng, A 2013;586:276–83. https://doi.org/10.1016/j.msea.2013.07.094.

[11] Park KT. Tensile deformation of low-density Fe–Mn–Al–C austenitic steels at ambient temperature. Scripta Mater 2013;68:375–9. https://doi.org/10.1016/j.scriptamat.2012.09.031.

[12] Gutierrez-Urrutia I, Raabe D. Multistage strain hardening through dislocation substructure and twinning in a high strength and ductile weight-reduced Fe–Mn–Al–C steel. Acta Mater 2012;60:5791–802. https://doi.org/10.1016/j.actamat.2012.07.018.

[13] Ma B, Li C, Zheng J, Song Y, Han Y. Strain hardening behavior and deformation substructure of Fe–20/27Mn–4Al–0.3C non-magnetic steels. Mater Des 2016;92:313–21. https://doi.org/10.1016/j.matdes.2015.12.038.

[14] Sohn SS, Song H, Suh BC, Kwak JH, Lee BJ, Kim NJ, Lee S. Novel ultra-high-strength (ferrite + austenite) duplex lightweight steels achieved by fine dislocation substructures (Taylor lattices), grain refinement, and partial recrystallization. Acta Mater 2015;96:301–10. https://doi.org/10.1016/j.actamat.2015.06.024.

[15] Zambrano OA. A general perspective of Fe–Mn–Al–C steels. J Mater Sci 2018;53:14003–62. https://doi.org/10.1007/s10853-018-2551-6.

[16] Chen EC, Chou CR, Li P, Chu SL. Effect of aluminium on TRIP Fe–Mn–A1 alloy steels at room temperature. Mater Sci Eng, A 1993;160:261–70. https://doi.org/10.1016/0921-5093(93)90455-N.

[17] Tian X, Tian R, Wei X, Zhang Y. Effect of Al content on work hardening in austenitic Fe–Mn–Al–C alloys. Can Metall Q 2004;43:183–92. https://doi.org/10.1179/cmq.2004.43.2.183.

[18] Abedi HR, Zarei-Hanzaki A, Ou KL, Yu CH. Substructure hardening in duplex low-density steel. Mater Des

2017;116:472–80. https://doi.org/10.1016/j.matdes.2016.12.020.
[19] Yoo JD, Park KT. Microband-induced plasticity in a high Mn–Al–C light steel. Mater Sci Eng, A 2008;496:417–24. https://doi.org/10.1016/j.msea.2008.05.042.
[20] Yoo JD, Hwang SW, Park KT. Origin of extended tensile ductility of a Fe–28Mn–10Al–1C steel. Metall Mater Trans A 2009;40:1520–3. https://doi.org/10.1007/s11661-009-9862-9.
[21] Gutierrez-Urrutia I, Raabe D. Influence of Al content and precipitation state on the mechanical behavior of austenitic high-Mn low-density steels. Scripta Mater 2013;68:343–7. https://doi.org/10.1016/j.scriptamat.2012.08.038.
[22] Sohn SS, Choi K, Kwak JH, Kim NJ, Lee S. Novel ferrite-austenite duplex lightweight steel with 77% ductility by transformation induced plasticity and twinning induced plasticity mechanisms. Acta Mater 2014;78:181–9. https://doi.org/10.1016/j.actamat.2014.06.059.
[23] Li S, Li D, Lu H, Cao P, Xie R. Effect of κ-carbides on deformation behavior of Fe–27Mn–10Al–1C low-density steel. Crystals 2022;12:991. https://doi.org/10.3390/cryst12070991.
[24] Liu M, Li X, Zhang Y, Song C, Zhai Q. Multiphase precipitation and its strengthening mechanism in a V-containing austenite-based low-density steel. Intermetallics 2021;134:107179. https://doi.org/10.1016/j.intermet.2021.107179.
[25] Kang L, Yuan H, Li H, Ji Y, liu H, Liu G. Enhanced mechanical properties of Fe–Mn–Al–C low-density steel via aging treatment. Front. Mater. 2021;8:680776. https://doi.org/10.3389/fmats.2021.680776.
[26] Li Z, Wang Y, Cheng X, Liang J, Li S. Compressive behavior of a Fe–Mn–Al–C lightweight steel at different strain rates. Mater Sci Eng, A 2020;772:138700. https://doi.org/10.1016/j.msea.2019.138700.
[27] Saeed-Akbari A, Imlau J, Prahl U, Bleck W. Derivation and variation in composition-dependent stacking fault energy maps based on subregular solution model in high-manganese steels. Metall Mater Trans A 2009;40:3076–90. https://doi.org/10.1007/s11661-009-0050-8.
[28] ASTM E209-18. Standard practice for compression tests of metallic materials at elevated temperatures with conventional or rapid heating rates and strain rates. Conshohocken, PA: ASTM International West; 2018. https://doi.org/10.1520/E0209-18.
[29] Abedi HR, Zarei-Hanzaki A, Liu Z, Xin R, Haghdadi N, Hodgson PD. Continuous dynamic recrystallization in low density steel. Mater Des 2017;114:55–64. https://doi.org/10.1016/j.matdes.2016.10.044.
[30] Kang S, Jung YS, Jun JH, Lee YK. Effects of recrystallization annealing temperature on carbide precipitation, microstructure, and mechanical properties in Fe–18Mn–0.6C–1.5Al TWIP steel. Mater Sci Eng, A 2010;527:745–51. https://doi.org/10.1016/j.msea.2009.08.048.
[31] Ji F, Song W, Ma Y, Li C, Bleck W, Wang G. Recrystallization behavior in a low-density high-Mn high-Al austenitic steel undergone thin strip casting process. Mater Sci Eng, A 2018;733:87–97. https://doi.org/10.1016/j.msea.2018.07.023.
[32] Wu H, Tan Y, Malik A, Wang Y, Naqvi SZH, Cheng H, Tian J, Meng X. Dynamic compressive mechanical behavior and microstructure evolution of rolled Fe–28Mn–10Al–1.2C low-density steel. Materials 2022;15:3550. https://doi.org/10.3390/ma15103550.
[33] Kuhlmann-Wilsdorf D. The theory of dislocation-based crystal plasticity. Philos Mag A 1999;79:955–1008. https://doi.org/10.1080/01418619908210342.
[34] Gutierrez-Urrutia I, Raabe D. Dislocation and twin substructure evolution during strain hardening of an Fe–22 wt.% Mn–0.6 wt.% C TWIP steel observed by electron channeling contrast imaging. Acta Mater 2011;59:6449–62. https://doi.org/10.1016/j.actamat.2011.07.009.
[35] Canadinc D, Sehitoglu H, Maier HJ, Chumlyakov YI. Strain hardening behavior of aluminum alloyed Hadfield steel single crystals. Acta Mater 2005;53:1831–42. https://doi.org/10.1016/j.actamat.2004.12.033.
[36] Canadinc D, Sehitoglu H, Maier HJ, Chumlyakov YI. Strain hardening behavior of aluminum alloyed Hadfield steel single crystals. Acta Mater 2005;53:1831–42. https://doi.org/10.1016/j.actamat.2004.12.033.
[37] Abedi HR, Hanzaki AZ, Haghdadi N, Hodgson PD. Substructure induced twinning in low density steel. Scripta Mater 2017;128:69–73. https://doi.org/10.1016/j.scriptamat.2016.10.001.
[38] Kishore K, Kumar RG, Chandan AK. Critical assessment of the strain-rate dependent work hardening behaviour of AISI 304 stainless steel. Mater Sci Eng, A 2021;803:140675. https://doi.org/10.1016/j.msea.2020.140675.
[39] del Valle JA, Carreño F, Ruano OA. Influence of texture and grain size on work hardening and ductility in magnesium-based alloys processed by ECAP and rolling. Acta Mater 2006;54:4247–59. https://doi.org/10.1016/j.actamat.2006.05.018.
[40] Akbarian S, Zarei-Hanzaki A, Abedi HR, Unnikrishnan R, Moat R. Substructure development and deformation twinning stimulation through regulating the processing path during multi-axial forging of twinning induced plasticity steel. Adv Eng Mater 2018;20:1800453. https://doi.org/10.1002/adem.201800453.
[41] Ma B, Li C, Zheng J, Song Y, Han Y. Strain hardening behavior and deformation substructure of Fe–20/27Mn–4Al–0.3C non-magnetic steels. Mater Des 2016;92:313–21. https://doi.org/10.1016/j.matdes.2015.12.038.
[42] Welsch E, Zaefferer S, Ponge D, Hafez Haghighat SM, Sandlobes S, Choi P, Herbig M, Raabe D. Strain hardening by dynamic slip band refinement in a high-Mn lightweight steel. Acta Mater 2016;116:188–99. https://doi.org/10.1016/j.actamat.2016.06.037.
[43] Gutierrez-Urrutia I, Raabe D. Multistage strain hardening through dislocation substructure and twinning in a high strength and ductile weight-reduced Fe–Mn–Al–C steel. Acta Mater 2012;60:5791–802. https://doi.org/10.1016/j.actamat.2012.07.018.
[44] Dong H, Sun X. Deformation induced ferrite transformation in low carbon steels. Curr Opin Solid State Mater Sci 2005;9:269–76. https://doi.org/10.1016/j.cossms.2006.02.014.
[45] Hong SC, Lim SH, Lee KJ, Shin DH, Lee KS. Effect of undercooling of austenite on strain induced ferrite transformation behavior. ISIJ Int 2003;43:394–9. https://doi.org/10.2355/isijinternational.43.394.
[46] Kalantari AR, Zarei-Hanzaki A, Abedi HR, Hassanpour-Esfahani M, Park SJ, Park JY. Microstructure evolution and room temperature mechanical properties of a thermomechanically processed ferrite-based low-density steel. Mater Sci Eng, A 2019;754:57–67. https://doi.org/10.1016/j.msea.2019.03.048.
[47] Kalantari AR, Zarei-Hanzaki A, Abedi HR, Park SJ, Park JY. Bi-directional ferrite to austenite transformation through warm temperature deformation of a ferrite-based low-density steel. Mater Sci Eng, A 2021;821:141596. https://doi.org/10.1016/j.msea.2021.141596.
[48] Timokhina IB, Hodgson PD, Pereloma EV. Effect of microstructure on the stability of retained austenite in transformation-induced-plasticity steels. Metall Mater Trans A 2004;35:2331–41. https://doi.org/10.1007/s11661-006-0213-9.